

**Antiferromagnetic Semiconductor $\text{Eu}_3\text{Sn}_2\text{P}_4$ with Sn-Sn Dimer and Crown-wrapped Eu**

Journal:	<i>Journal of Materials Chemistry C</i>
Manuscript ID	TC-ART-07-2019-003557.R2
Article Type:	Paper
Date Submitted by the Author:	26-Aug-2019
Complete List of Authors:	Blawat, Joanna ; Louisiana State University, Chemistry Swatek, Przemyslaw ; Ames Laboratory Gui, Xin; Louisiana State University, Chemistry Jin, Rongying; Louisiana State University, Physics Xie, Weiwei; Louisiana State University, Chemistry

Antiferromagnetic Semiconductor $\text{Eu}_3\text{Sn}_2\text{P}_4$ with Sn-Sn Dimer and Crown-wrapped Eu

Joanna Blawat^{1,2}, Przemyslaw Swatek^{3,4,5}, Xin Gui¹, Rongying Jin^{2*}, Weiwei Xie^{1*}

¹ Department of Chemistry, Louisiana State University, Baton Rouge, LA 70803, USA

² Department of Physics and Astronomy, Louisiana State University, Baton Rouge, LA 70803, USA

³ Division of Materials Science and Engineering, Ames Laboratory, Ames, Iowa 50011, USA

⁴ Department of Physics and Astronomy, Iowa State University, Ames, Iowa 50011, USA

⁵ Institute of Low Temperature and Structure Research, Polish Academy of Sciences, P.O. Box 1410, 50-950 Wroclaw, Poland

ABSTRACT

A novel antiferromagnetic semiconductor, $\text{Eu}_3\text{Sn}_2\text{P}_4$, has been discovered. Single crystals of $\text{Eu}_3\text{Sn}_2\text{P}_4$ were prepared using the Sn self-flux method. The crystal structure determined by single crystal X-ray diffraction shows that $\text{Eu}_3\text{Sn}_2\text{P}_4$ crystallizes in the orthorhombic structure with space group *Cmca* (Pearson Symbol, *oP216*). Six Sn-Sn dimers connected by P atoms form $\text{Sn}_{12}\text{P}_{24}$ crown-shape clusters with Eu atoms located in the center. Magnetization measurements indicate that the system orders antiferromagnetically below $T_N \sim 14$ K at low field and undergoes a metamagnetic transition at high field when $T < T_N$. The effective magnetic moment is $7.41(3)\mu_B/\text{Eu}$, corresponding to Eu^{2+} . The electric resistivity reveals non-monotonic temperature dependence with non-metallic behavior below ~ 60 K, consistent with the band structure calculations. By fitting the data using the thermally activated resistivity formula, we estimate energy gap ~ 0.14 eV. Below T_N , the resistivity tends to saturate, suggesting the reduction of charge-spin scattering.

1 Introduction

2 Magnetic semiconductors with a combination of magnetic response and semiconducting
3 properties, if implemented in a device, could provide a new way to control electronics. Research
4 has been mainly focused on the magnetically doped semiconductor, such as Mn-doped GaAs and
5 magnetic semiconducting heterostructures in which material fabrication, experimental
6 measurement and property optimization are quite challenging.¹ Little progress has been made in
7 identifying intrinsic bulk magnetic semiconductors. Among several reported magnetic
8 semiconductors, europium chalcogenides, EuCh (Ch= O and S), are particularly attractive. In
9 addition to the ideal Heisenberg ferromagnets with high magnetic moments ($\sim 7\mu_B$) and simple
10 NaCl-type rocksalt structure, EuCh exhibits also intriguing optical and electrical properties. For
11 example, large Faraday and Kerr effects have been observed, making EuO promising for magneto-
12 optical sensor applications.²⁻⁶ With increasing the atomic number of Ch, the Curie-Weiss
13 temperatures θ_{CW} decrease^{7,8} dramatically from EuO to EuSe. ($T_C = 69.3$ K for EuO, 16.6 K for
14 EuS, and -4.6 K for EuSe). The Curie-Weiss temperature of thin-film ferromagnetic Eu₃P₂ and
15 Eu₃As₂ is 25.0 K and 17.3 K, respectively.^{9,10} These indicate that magnetic interaction between Eu
16 moments is strongly influenced by liganded main group atoms. For potential applications, it is
17 highly desirable if ligand atoms can enhance magnetic interaction so to form magnetic ordering at
18 room temperature.

19 The strategy to design new magnetic semiconductors is to introduce Eu into Zintl phases, which
20 are valence-precise compounds consisting of electropositive elements and electronegative
21 polyanions.^{11,12} This has been proved to be a useful empirical rule to make new semiconductors or
22 semimetals. For example, BaGa₂P₂ and EuGa₂P₂ crystalize in the similar crystal structure and the
23 later shows magnetic ordering with negative magnetoresistance (MR).^{13,14} New Zintl phases,
24 Ba₃Ga₂P₄, Sr₃Sn₂P₄, and Sr₃Si₂As₄ were reported to adopt one-dimensional chain structures. Later,
25 Eu₃Ga₂P₄ was discovered in which the structure is derived by partial substitution of Eu for some
26 Ga-Ga dumbbells.¹⁵ In addition, a similar Zintl compound, Eu₃In₂P₄, is reported to be a
27 semiconductor with an energy gap of 0.42-0.45 eV and a magnetic transition at 14.5 K.¹⁴ The
28 question arises whether Eu₃Sn₂P₄ can be synthesized.

29 In this article, we report the single crystal growth of new magnetic Zintl compound Eu₃Sn₂P₄
30 using the Sn self-flux. Eu₃Sn₂P₄ was determined to be orthorhombic with the space group *Cmca*,
31 which is isostructural to Sr₃Sn₂P₄. Magnetic measurements demonstrate an antiferromagnetic
32 transition (T_N) around 14 K. The high-temperature data (50-300K) can be fitted using the Curie-
33 Weiss law, which gives $\Theta = 6.5(2)$ K with an effective magnetic moment $\sim 7.41(3)\mu_B/\text{Eu}$. The
34 electric resistivity measurements and band structure calculations confirm the semiconducting
35 character.

36

1 Experimental Techniques

2 Single crystalline $\text{Eu}_3\text{Sn}_2\text{P}_4$ was grown using the Sn self-flux method with the initial molar ratio
3 of Eu: Sn: P = 3: 30: 4. The high purity elements, Eu ingot (99.9%), phosphorus lump (99.999%),
4 and tin granules (99.9%), were put into an alumina crucible and sealed into a quartz tube. The
5 ampoule was heated up to 600 °C at a rate of 60 °C/h and kept at 600 °C for 5 hours to avoid
6 explosion of phosphorus. Then, the sample was heated up to 1050°C at a rate of 60°C/h and held
7 for 5 hours followed by slow cooling (at a rate of 5°C/h) to 600 °C. The Sn flux was centrifuged
8 into quartz wool at 600 °C. Typical single crystals have dimensions of $\sim 0.5 \times 0.5 \times 0.5 \text{ mm}^3$.

9 The structure of $\text{Eu}_3\text{Sn}_2\text{P}_4$ single crystals was determined using a Bruker Apex II single X-ray
10 diffractometer equipped with Mo radiation ($\lambda_{\text{K}\alpha} = 0.71073 \text{ \AA}$). The crystal structure was refined
11 by the full-matrix least-squares method using the SHELXLTL package.¹⁶ The sample was further
12 examined by powder X-ray diffraction using Rigaku MiniFlex 600 diffractometer with Cu
13 $\text{K}_{\alpha 1}$ radiation ($\lambda = 1.5406 \text{ \AA}$). Data was collected in the 2θ range 5 to 90° with step 0.005°. The
14 lattice parameters were obtained by using Le Bail fitting with FullProf software.¹⁷ The chemical
15 composition was also checked by the Scanning Electron Microscope (JSM-6610 LV) equipped
16 with Energy-Dispersive Spectrometer (EDS). The spectrum was collected on several locations on
17 the $\text{Eu}_3\text{Sn}_2\text{P}_4$ single crystal using an accelerating voltage 20 kV and time 50s. EDS data were
18 analyzed using EDAX TEAM software. Magnetic measurements were performed in a Quantum
19 Design Magnetic Properties Measurement System (MPMS). The susceptibility measurements
20 were carried out in zero field cooling (ZFC) and field cooling (FC) modes. A Quantum Design
21 Physical Property Measurement System (PPMS) was used to measure the electrical resistivity
22 using the standard AC four-probe technique. The specific heat was measured using the relaxation
23 method.

24 The scalar relativistic electronic structure calculations were carried out using the full-potential
25 local-orbital minimum-basis band structure scheme (FPLO)^{18,19} The Perdew and Wang exchange-
26 correlation potential was employed.²⁰ Strong Coulomb repulsion (U) in the Eu 4*f* orbitals was
27 treated using the local spin density approximation in the atomic-limit double counting scheme of
28 the Local Spin Density Approximation (LSDA) with the unrestricted Hartree-Fock (UHF)
29 approximation (LSDA+ U).^{21,22} There exists no spectroscopy data for $\text{Eu}_3\text{Sn}_2\text{P}_4$, therefore,
30 throughout this work, the arbitrarily values of on-site Coulomb repulsion $U = 5 \text{ eV}$ and the on-site
31 exchange $J = 1 \text{ eV}$ were adopted to account for the strongly localized Eu-4*f* orbitals.^{23,24} Due to a
32 large number of atoms and very likely complex antiferromagnetic structure, a simple lower
33 symmetrical model was applied to allow for the possibility of magnetic ordering within the given
34 unit cell. The energies were converged on the Monkhorst-Pack grid with $3 \times 3 \times 2$ points using
35 the tetrahedron method.²⁵ This approach provided a good agreement with presented experimental
36 data.

37

38

1 Results and Discussion

2 Details of refinement performed on single-crystal X-ray diffraction data are presented in Table 1.
 3 The results indicate that $\text{Eu}_3\text{Sn}_2\text{P}_4$ crystallizes in an orthorhombic crystal structure (*Cmca*, No.64)
 4 with lattice parameters $a = 24.882(3)$ Å, $b = 12.453(2)$ Å and $c = 18.493(2)$ Å. The atomic
 5 coordinates, isotropic displacement parameters, and anisotropic thermal displacement parameters
 6 are summarized in Table 2 and Table S1, respectively. The short Sn-Sn distance in $\text{Eu}_3\text{Sn}_2\text{P}_4$
 7 [$d(\text{Sn1-Sn3}) = 2.7472(6)$ Å, $d(\text{Sn2-Sn2}) = 2.7838(8)$ Å] indicates the strong atomic interactions
 8 between Sn and Sn. Similarly, short distances between Sn and Sn were observed in β -Sn in SrSn_4
 9 - $d(\text{Sn-Sn}) = 3.0328$ Å and $d(\text{Sn-Sn}) = 2.9044$ Å, respectively, which is called “dimer”. Thus, we
 10 can treat Sn-Sn as a dimer in $\text{Eu}_3\text{Sn}_2\text{P}_4$, which is shown in Figure 1(a). The Sn-Sn dimer is
 11 surrounded by six P atoms and forms $[\text{Sn}_2\text{P}_6]$ octahedra (see Figure 1(b)). Four of six P atoms in
 12 $[\text{Sn}_2\text{P}_6]$ octahedra connect with neighboring $[\text{Sn}_2\text{P}_6]$ octahedra. This arrangement results in a
 13 unique $[\text{Sn}_{12}\text{P}_{24}]$ double layered six-membered ring, which helps build the “crown-like” anion
 14 clusters in $\text{Eu}_3\text{Sn}_2\text{P}_4$ (see Figure 1(c)). As can be seen inside the anion of $[\text{Sn}_{12}\text{P}_{24}]^{36-}$ is
 15 encapsulated a cation of Eu^{2+} . As a result, the crystal structure of $\text{Eu}_3\text{Sn}_2\text{P}_4$ can be considered as a
 16 polyanionic network of $[\text{Sn}_{12}\text{P}_{24}]^{36-}$, which is presented in Figure 1(d) along *c* crystallographic
 17 axis. The $[\text{Sn}_{12}\text{P}_{24}]^{36-}$ anion is marked using the green dashed line. The whole structure of $\text{Eu}_3\text{Sn}_2\text{P}$
 18 built from $[\text{Sn}_{12}\text{P}_{24}]^{36-}$ anion with Eu cation inside is presented on Figure 1 (e) along the *c*
 19 crystallographic axis. Combined with the electric resistivity measurements below, the semimetallic
 20 $\text{Eu}_3\text{Sn}_2\text{P}_4$ can be considered as $(\text{Eu}^{2+})_3(\text{Sn}_2)^{2-}(\text{P}^{3-})_4$ according to the Zintl concept. The same crystal
 21 structure were reported in two Sr-based compounds: $\text{Sr}_3\text{Sn}_2\text{P}_4$ ²⁶ and α - $\text{Sr}_3\text{Sn}_2\text{As}_4$.²⁷ The powder
 22 XRD pattern is presented in Figure 2. The calculated pattern based on refinement obtained from
 23 single crystal X-ray diffraction was generated using Fullprof software. The pattern obtained
 24 experimentally matches with generated one, which confirms the $\text{Eu}_3\text{Sn}_2\text{P}_4$ phase.

25 Figure 3(a) exhibits the temperature dependence of magnetic susceptibility measured on $\text{Eu}_3\text{Sn}_2\text{P}_4$
 26 single crystals under applied field $\mu_0H = 0.1$ T. In the main panel, the susceptibility increases with
 27 decreasing temperature and exhibit paramagnetic behavior. In the low temperatures, there is
 28 observed a sharp maximum around $T_N \sim 14$ K, which indicate the antiferromagnetic phase
 29 transition (marked by arrow in Figure 3(a)). There is no significant change between zero field
 30 cooling (ZFC) and field cooling (FC) curve. In the inset in Figure 3(a) is presented the temperature
 31 dependence of inverse susceptibility. The experimental data follow the Curie-Weiss law (red solid
 32 line in Figure. 3(a)), $\chi(T) = C/(T - \theta)$, where θ is paramagnetic Curie temperature and C is Curie
 33 constant with $C = \frac{\mu_{\text{eff}}^2 N_A}{3k_B}$, where N_A is Avogadro constant, k_B is Boltzmann constant. Hence, the
 34 effective magnetic moment can be calculated using the formula $\mu_{\text{eff}} = \sqrt{8C}$, and the obtained fitting
 35 parameters are: $\theta = 6.5(2)$ K and $\mu_{\text{eff}} = 7.41(3)$ μ_B . The estimated effective magnetic moment is
 36 close to the theoretical value for Eu^{2+} free ion predicted by Russell-Saunders coupling scenario
 37 ($\mu_{\text{eff}} = 7.94\mu_B$), and indicate that 4*f* electrons are well localized. The positive sign of obtained
 38 paramagnetic Curie-Weiss temperature θ suggests that there is ferromagnetic interaction between
 39 Eu ions. However, as we can see in the main panel of Figure 3(a) the compound orders

1 antiferromagnetically with $T_N \sim 14$ K. Similar behavior was observed in many different Eu-based
 2 compounds, such as EuSnP^{28} , $\text{EuCr}_2\text{Al}_{20}^{29}$, and $\text{Eu}_3\text{In}_2\text{P}_4^{14}$. The long-range antiferromagnetic
 3 ordering with positive Curie-Weiss temperature was also observed for some Eu compounds in
 4 $\text{Ca}_3\text{Si}_2\text{As}_4$ -structure type, for example, $\text{Eu}_3\text{Ge}_2\text{As}_4$ and $\text{Eu}_3\text{Si}_2\text{As}_4$.³⁰ It is also worth noting that in
 5 $\text{Eu}_3\text{Sn}_2\text{P}_4$ there exist 7 different Wyckoff positions (see Table 2), which may lead to a complex
 6 magnetic structure in low temperatures.

7 The magnetization versus magnetic field measured at different temperatures is presented in Figure
 8 3(b). At high temperatures, M increases linearly with increasing H . However, below 40 K, $M(H)$
 9 becomes non-linear. The magnetization in the stronger field shows a tendency to saturation and
 10 reaches the value $M = 2.7 \times 10^4$ emu/mol_{Eu} at 7 T and 2 K, which correspond to the magnetic
 11 moment of $5.17\mu_B$. This is smaller than the theoretically predicted saturation moment ($\mu_{\text{sat}} = 7\mu_B$)
 12 calculated for three ion Eu^{2+} per formula. The $M(H)$ curves below T_N are presented in Figure 3(c).
 13 The magnetization deviates from linearity around H_1 with a faster increase at $H > H_1$ and then slows
 14 down when $H > H_2$. This indicates that there is a metamagnetic transition, which is marked by
 15 arrows in Figure 3(c). The changes in transition fields versus temperature are shown in Figure 3(d).
 16 H_1 and H_2 shift towards a weaker magnetic field with increasing temperatures.

17 The temperature dependence of the electrical resistivity ρ is shown in Figure 4. At room
 18 temperature, the electrical resistivity is $\rho = 194$ m Ω cm, which is lower than observed in other Eu-
 19 based semiconductor $\text{Eu}_3\text{In}_2\text{P}_4$ (~ 500 m Ω cm), and higher than in elemental metals like copper (ρ
 20 $= 1.72 \times 10^{-3}$ m Ω cm).^{31,32} The positive sign of $d\rho/dT$ suggests the metallic behavior of the
 21 compound, the resistivity value is high. Around $T \sim 60$ K the electrical resistivity reaches the
 22 minimum and then increases with decreasing temperature. This clearly indicates that $\text{Eu}_3\text{Sn}_2\text{P}_4$ has
 23 a non-metallic ground state. The low-temperature data were fitted using the formula:

$$24 \quad \rho = \rho_0 + AT + B \exp(-\Delta/2k_B T), \quad (1)$$

25 where ρ_0 is the residual resistivity, A and B are temperature independent constants, and k_B is the
 26 Boltzmann constant. The 2nd term represents the metallic scattering channel ($\sim AT$), and the 3rd
 27 term describes thermally-activated semiconducting contribution with Δ the activation energy
 28 [$\sim B \exp(-\Delta/2k_B T)$].^{33,34} The fit yields to the parameters: $\rho_0 = 168(1)$ m Ω cm, $A = 0.06(1)$ m Ω cm
 29 K^{-1} , $B = 47.8(8)$ m Ω cm and $\Delta = 0.14(1)$ eV. The energy gap is smaller than in other Eu-based
 30 magnetic semiconductor, such as $\text{Eu}_3\text{In}_2\text{P}_4$ ($\Delta = 0.452$ eV) or $\text{Eu}_3\text{Ga}_2\text{P}_4$ ($\Delta = 0.552$ eV).^{32,35} In the
 31 inset in Figure 4 is shown the low-temperature range of electrical resistivity. Below T_N , $\rho(T)$
 32 becomes saturated with $\rho = 197$ m Ω cm.

33 The temperature dependence of the specific heat measured in the range from 1.9 to 200 K is shown
 34 on the main panel in Figure 5(a). The lambda-shape anomaly is observed at $T_N = 14$ K, confirming
 35 the phase transition in $\text{Eu}_3\text{Sn}_2\text{P}_4$. The jump in specific heat (ΔC) at T_N is equal to 8.3 J/(mol/_{Eu} K).
 36 According to the mean-field theory, the jump ΔC expected for simple equal-moment
 37 antiferromagnet (EM-AFM) can be calculated using the formula: $\Delta C = \frac{5J(J+1)}{2J^2+2J+1}R$,³⁶ where J is
 38 total angular momentum and R is the gas constant. For three ions of Eu^{2+} with $J \sim S \sim 7/2$, $\Delta C = 20.14$

1 J/(mol/Eu K), which is significantly larger than observed for $\text{Eu}_3\text{Sn}_2\text{P}_4$, which may be related to
2 the complex magnetic structure. The temperature dependence of specific heat measured in a
3 different applied magnetic field is presented in the inset in Figure 5(a). The transition temperature
4 shifts towards lower temperatures with increasing magnetic field and at 5 T is completely
5 suppressed. In specific heat $C(T)/T$ there is a hump around $T = 5$ K, which can be attributed to
6 Zeeman splitting.³⁷ The hump in $C(T)/T$ below T_N arises naturally within MFT for large S .³⁷
7 Similar hump in $C(T)/T$ was previously observed in other Eu-based compounds like $\text{Eu}_3\text{In}_2\text{P}_4$,¹⁴
8 $\text{EuCr}_2\text{Al}_{20}$ ²⁹ or the series EuTGe_3 ($T = \text{Ni, Pd, Pt, Co}$).³⁸ The calculated entropy in the low-
9 temperature range is presented in Figure 5(b). The entropy released at T_N is 10 J/(mol/Eu K) and is
10 reduced by 58% from expected value for the 8-fold degenerated system $S = R\ln(2J+1) = R\ln 8 =$
11 17.28 J/(mol/Eu K) per mole of Eu. Worth noting is an extended tail in specific heat above T_N ,
12 which together with reduced entropy indicate for short-range interaction in complex
13 antiferromagnetic structure.³⁹

14 Figures 6 (a) and (b) present the density of states (DOS) and band structure of $\text{Eu}_3\text{Sn}_2\text{P}_4$ calculated
15 using the full-potential non-orthogonal local-orbital code (FPLO) with the with an additional
16 Hubbard-like term parameterized with $U = 5$ eV and $J = 1$ eV. Since the detailed experimental
17 magnetic structure is unknown, we compared an antiferromagnetic (parallel coupling of the spins
18 within the magnetic layer, antiparallel interlayer alignments) as well as a ferromagnetic (not
19 shown) patterns of the Eu-4*f* magnetic moments. The total energies of the both models indicate
20 that the applied AFM model is lower in energy and thus more stable (the energy difference between
21 AFM and FM model is equal to 167 meV/f.u.).

22 In agreement with the previous calculations for $\alpha\text{-Sr}_3\text{Sn}_2\text{As}_4$, the ground state of $\text{Eu}_3\text{Sn}_2\text{P}$ is a
23 directly gapped semiconductor with an anisotropic electron transport, mainly along the stacking
24 direction. The separation between the top of the valence band and the bottom of the conduction
25 band is about 0.15 eV at the Γ point e.g, less than one-quarter the values 0.87 for the isostructural
26 $\alpha\text{-Sr}_3\text{Sn}_2\text{As}_4$.²⁷ This result fully corroborates with the semiconducting nature of $\text{Eu}_3\text{Sn}_2\text{P}_4$, as
27 suggested by transport measurements, and can further benefit in the flexibility of both doping and
28 alloying on the cation Eu^{2+} sites by slightly perturbing the anionic network. The presence of the
29 gap in the vicinity of the Fermi level is a characteristic feature of many Zintl phases.^{8,9, 40} Many
30 series of these compounds, for example BaCaX ($X = \text{Si, Ge, Sn and Pb, Group IV}$), XNiSn and
31 XCoSb ($X = \text{Ti, Zr or Hf}$), $\text{AELi}_2\text{In}_2\text{Ge}_2$ ($\text{AE} = \text{Sr, Ba, Eu}$), exhibit a crossover from
32 semiconducting to metallic behavior upon doping or alloying with larger atomic sizes and heavier
33 atoms.^{41–43}

34 It should be noted that varying U value does not change qualitatively results of the electronic
35 structure calculations in $\text{Eu}_3\text{Sn}_2\text{P}_4$. However, the size of the gap is sensitive to the value of the U
36 parameter, due to changes of the energy separation, e.g. LSDA+ U potential opens a band gap in
37 AFM $\text{Eu}_3\text{Sn}_2\text{P}_4$ (with broken symmetry), while LSDA does not.

38 Figure 6 (a) shows general shapes of the total and partial DOSs, which also closely resemble the
39 electronic structure of non-magnetic $\beta\text{-Sr}_3\text{Sn}_2\text{As}_4$ system, apart from obvious differences

1 associated with the different infinite chains ligand.²⁷ As we analyze above, the cation-anion
2 interactions in both compounds are not exactly the same, and the anion of $[\text{Sn}_{12}\text{P}_{24}]^{36-}$ cation of
3 Eu^{2+} bonds in $\text{Eu}_3\text{Sn}_2\text{P}_4$ imply a slightly higher degree of covalency resulting in a narrower band
4 gap. Nevertheless, the results of DOS indicate nearly optimized bonding interactions consistent
5 with the classical picture for Zintl compounds. The key difference between nonmagnetic α -
6 $\text{Sr}_3\text{Sn}_2\text{As}_4$ and $\text{Eu}_3\text{Sn}_2\text{P}_4$ is the presence of a fairly narrow Eu-4*f* states in the central portion of the
7 valence band at around -0.7 eV below E_F , meaning that the Eu-4*f* can be considered as localized
8 states that play a secondary role in the bonding in $\text{Eu}_3\text{Sn}_2\text{P}_4$.^{11,44,45} The presence of spin splitting
9 only for Eu-4*f* orbitals resemble antiferromagnetic ground state and specifies the existence of
10 magnetic moment localized almost entirely at the europium cations. In both spin arrangements, the
11 Eu-4*f* occupation at each Wyckoff position is close to seven and spin-moments of $S = 7 \mu\text{B}$ per Eu
12 atom, which is consistent with the experimental magnetic data. Finally, high degree of localization
13 of Eu-4*f* ions in $\text{Eu}_3\text{Sn}_2\text{P}_4$ is also supported by the fact that the shortest Eu–Eu bond distance in
14 this compound is comparable to other reported intermetallic compounds containing of the divalent
15 Eu ions, such as EuGe_2 ,⁴⁶ EuGa_2P_2 ,^{10, 12} EuSnP ,⁴⁷ EuPd_3B_x ⁴⁸ etc. Therefore, the localized
16 character of the Eu-4*f* electrons in these compounds might be a consequence of expected negligible
17 direct f-f magnetic exchange interactions and very weak f -ligand hybridization (Eu atoms are
18 located inside in a highly symmetric anion of $[\text{Sn}_{12}\text{P}_{24}]^{36-}$ with closed outer electronic shells.⁴⁹

19 **Conclusion**

20 The single crystals of novel $\text{Eu}_3\text{Sn}_2\text{P}_4$ compound were synthesized using self-flux method and its
21 crystal structure and physical properties were determined. $\text{Eu}_3\text{Sn}_2\text{P}_4$ crystallizes in an
22 orthorhombic crystal structure (*Cmca*, No. 64) with lattice parameter: $a = 24.882(3) \text{ \AA}$, $b =$
23 $12.453(2) \text{ \AA}$ and $c = 18.493(2) \text{ \AA}$. The compound shows Curie-Weiss behavior with well localized
24 europium 4*f* electrons and orders antiferromagnetically at $T_N \sim 14 \text{ K}$, which was confirmed by
25 susceptibility and specific heat measurements. However, reduced jump in specific heat, extended
26 short-range ordering above T_N and positive value of Curie-Weiss temperature indicate likely
27 complex magnetic structure of $\text{Eu}_3\text{Sn}_2\text{P}_4$. Electrical resistivity measurements and band calculation
28 confirmed the semiconducting properties of this material.

29 **Supporting Information**

30 Electronic supplementary information (ESI) available. See DOI: xxx

31 Crystallographic anisotropic thermal displacements and SEM data.

32 **Author Information**

33 Corresponding Author: weiweix@lsu.edu; rjin@lsu.edu

34 Notes: The authors declare no competing financial interest.

35 **Conflicts of interest**

36 There are no conflicts to declare

1 **Acknowledgement**

2 J. B. is supported by the State of Louisiana-Board of Regents Research Competitiveness
3 Subprogram (RCS) under Contract Number LEQSF(2017-20)-RD-A-08. W. X. is supported by
4 Beckman Young Investigator (BYI) Program. X.G. is supported by the National Science
5 Foundation under NSF-OIA-1832967. R. J. were supported by the DOE DE-SC0016315. P.S.'s
6 work at Ames Laboratory (electronic structure calculations) was supported by the U.S. Department
7 of Energy, Office of Basic Energy Sciences, Division of Materials Science and Engineering, and
8 the Interdisciplinary Centre for Mathematical and Computational Modelling (ICM) University of
9 Warsaw under grant no GB76-4, and at the Wrocław Centre for Networking and Supercomputing
10 under grant no. 359. Ames Laboratory is operated for the US Department of Energy by Iowa State
11 University under Contract No. DE-AC02-07CH11358.

1 References

- 2 1 T. Dietl, *Science*, 2000, **287**, 1019–1022.
- 3 2 Kie Ahn and J. Suits, *IEEE Trans. Magn.*, 1967, **3**, 453–455.
- 4 3 K. Y. Ahn and M. W. Shafer, *J. Appl. Phys.*, 1970, **41**, 1260–1262.
- 5 4 J. C. Suits, B. E. Argyle and M. J. Freiser, *J. Appl. Phys.*, 1966, **37**, 1391–1397.
- 6 5 D. B. Ghosh, M. De and S. K. De, *Phys. Rev. B*, 2004, **70**, 115211.
- 7 6 F. Liu, T. Makino, T. Yamasaki, K. Ueno, A. Tsukazaki, T. Fukumura, Y. Kong and M.
- 8 Kawasaki, *Phys. Rev. Lett.*, 2012, **108**, 257401.
- 9 7 L. Passell, O. W. Dietrich and J. Als-Nielsen, *Phys. Rev. B*, 1976, **14**, 4897–4907.
- 10 8 B. T. Matthias, R. M. Bozorth and J. H. Van Vleck, *Phys. Rev. Lett.*, 1961, **7**, 160–161.
- 11 9 G. Busch, F. Hulliger, P. Streit, P. Wachter and J. Wullschleger, *J. Phys. Colloq.*, 1971, **32**,
- 12 C1-734-C1-735.
- 13 10 G. Busch, M. Campagna, F. Hulliger and H. C. Siegmann, *J. Phys. Chem. Solids*, 1971, **32**,
- 14 2173–2179.
- 15 11 S. M. Kauzlarich, S. R. Brown and G. J. Snyder, *Dalton Trans.*, 2007, **0**, 2099–2107.
- 16 12 G. A. Papoian and R. Hoffmann, *Angew. Chem. Int. Ed.*, 2000, **39**, 2408–2448.
- 17 13 H. He, R. Stearrett, E. R. Nowak and S. Bobev, *Inorg. Chem.*, 2010, **49**, 7935–7940.
- 18 14 J. Jiang, M. M. Olmstead, S. M. Kauzlarich, H.-O. Lee, P. Klavins and Z. Fisk, *Inorg. Chem.*,
- 19 2005, **44**, 5322–5327.
- 20 15 N. Tsujii, C. A. Uvarov, P. Klavins, T. Yi and S. M. Kauzlarich, *Inorg. Chem.*, 2012, **51**,
- 21 2860–2866.
- 22 16 G. M. Sheldrick, *Acta Crystallogr. Sect. C Struct. Chem.*, 2015, **71**, 3–8.
- 23 17 J. Rodríguez-Carvajal, *Phys. B Condens. Matter*, 1993, **192**, 55–69.
- 24 18 K. Koepernik and H. Eschrig, *Phys. Rev. B*, 1999, **59**, 1743–1757.
- 25 19 K. Koepernik, B. Velický, R. Hayn and H. Eschrig, *Phys. Rev. B*, 1997, **55**, 5717–5729.
- 26 20 J. P. Perdew and Y. Wang, *Phys. Rev. B*, 1992, **45**, 13244–13249.
- 27 21 S. L. Dudarev, G. A. Botton, S. Y. Savrasov, C. J. Humphreys and A. P. Sutton, *Phys. Rev. B*,
- 28 1998, **57**, 1505–1509.
- 29 22 A. I. Liechtenstein, V. I. Anisimov and J. Zaanen, *Phys. Rev. B*, 1995, **52**, R5467–R5470.
- 30 23 I. Bigun, S. Steinberg, V. Smetana, Y. Mudryk, Y. Kalychak, L. Havela, V. Pecharsky and A.-
- 31 V. Mudring, *Chem. Mater.*, 2017, **29**, 2599–2614.
- 32 24 S. Steinberg, N. Card and A.-V. Mudring, *Inorg. Chem.*, 2015, **54**, 8187–8196.
- 33 25 H. J. Monkhorst and J. D. Pack, *Phys. Rev. B*, 1976, **13**, 5188–5192.
- 34 26 B. Eisenmann and U. Rößler, *Z. Für Anorg. Allg. Chem.*, 1998, **624**, 406–410.
- 35 27 X.-C. Liu, M.-Y. Pan, X. Li, S.-Q. Xia and X.-T. Tao, *Inorg Chem Front*, 2014, **1**, 689–694.
- 36 28 A. C. Payne, A. E. Sprauve, A. P. Holm, M. M. Olmstead, S. M. Kauzlarich and P. Klavins, *J.*
- 37 *Alloys Compd.*, 2002, **338**, 229–234.
- 38 29 P. Swatek and D. Kaczorowski, *J. Magn. Magn. Mater.*, 2016, **416**, 348–352.
- 39 30 X.-C. Liu, S.-Q. Xia, X.-W. Lei, M.-Y. Pan and X.-T. Tao, *Eur. J. Inorg. Chem.*, 2014, **2014**,
- 40 2248–2253.
- 41 31 R. A. Matula, *J. Phys. Chem. Ref. Data*, 1979, **8**, 1147–1298.
- 42 32 J. Jiang, M. M. Olmstead, S. M. Kauzlarich, H.-O. Lee, P. Klavins and Z. Fisk, *Inorg. Chem.*,
- 43 2005, **44**, 5322–5327.
- 44 33 R. A. Matula, *J. Phys. Chem. Ref. Data*, 1979, **8**, 1147–1298.
- 45 34 K. J. Laidler, *J. Chem. Educ.*, 1984, **61**, 494.

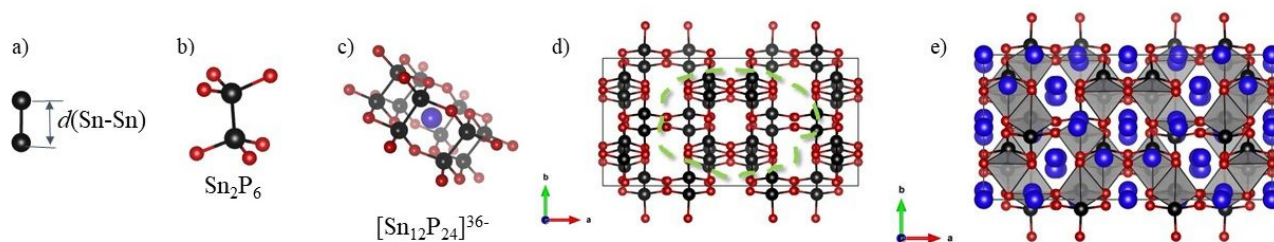
- 1 35 N. Tsujii, C. A. Uvarov, P. Klavins, T. Yi and S. M. Kauzlarich, *Inorg. Chem.*, 2012, **51**,
2 2860–2866.
- 3 36 J. A. Blanco, D. Gignoux and D. Schmitt, *Phys. Rev. B*, 1991, **43**, 13145–13151.
- 4 37 D. C. Johnston, *Phys. Rev. B*, 2015, **91**, 064427.
- 5 38 O. Bednarchuk, A. Gagor and D. Kaczorowski, *J. Alloys Compd.*, 2015, **622**, 432–439.
- 6 39 *Handbook on the Physics and Chemistry of Rare Earths*, Elsevier, 2004.
- 7 40 J. Wang, M. Yang, M.-Y. Pan, S.-Q. Xia, X.-T. Tao, H. He, G. Darone and S. Bobev, *Inorg.*
8 *Chem.*, 2011, **50**, 8020–8027.
- 9 41 L.-L. Wang, A. Kaminski, P. C. Canfield and D. D. Johnson, *J. Phys. Chem. C*, 2018, **122**,
10 705–713.
- 11 42 W. G. Zeier, J. Schmitt, G. Hautier, U. Aydemir, Z. M. Gibbs, C. Felser and G. J. Snyder, *Nat.*
12 *Rev. Mater.*, 2016, **1**, 16032.
- 13 43 A. Ovchinnikov and S. Bobev, *Inorg. Chem.*, 2019, **58**, 7895–7904.
- 14 44 T.-S. You and G. J. Miller, *Inorg. Chem.*, 2009, **48**, 6391–6401.
- 15 45 T.-S. You, Y. Grin and G. J. Miller, *Inorg. Chem.*, 2007, **46**, 8801–8811.
- 16 46 S. Bobev, E. D. Bauer, J. D. Thompson, J. L. Sarrao, G. J. Miller, B. Eck and R.
17 Dronskowski, *J. Solid State Chem.*, 2004, **177**, 3545–3552.
- 18 47 X. Gui, G. J. Finkelstein, D. E. Graf, K. Wei, D. Zhang, R. E. Baumbach, P. Dera and W. Xie,
19 *Dalton Trans.*, 2019, **48**, 5327–5334.
- 20 48 R. Gumeniuk, M. Schmitt, C. Loison, W. Carrillo-Cabrera, U. Burkhardt, G. Auffermann, M.
21 Schmidt, W. Schnelle, C. Geibel, A. Leithe-Jasper and H. Rosner, *Phys. Rev. B*, ,
22 DOI:10.1103/PhysRevB.82.235113.
- 23 49 P. Aynajian, E. H. da Silva Neto, A. Gyenis, R. E. Baumbach, J. D. Thompson, Z. Fisk, E. D.
24 Bauer and A. Yazdani, *Nature*, 2012, **486**, 201–206.

25

26

1 **Figure 1.** The crystal structure of $\text{Eu}_3\text{Sn}_2\text{P}_4$. The solid black is the outline of unit cell, and the blue,
 2 red and black balls represent the Eu, P and Sn atoms. Figure (a): the Sn-Sn dimer. Figure (b):
 3 Sn_2P_6 octahedra. Figure (c): the single anion of $[\text{Sn}_{12}\text{P}_{24}]^{36-}$ with encapsulated Eu^{2+} cation. The
 4 drawing shows the view along c axis (Figure (d)) with a frame built from $[\text{Sn}_{12}\text{P}_{24}]^{36-}$ anions, and
 5 dashed green line represent a structure of one anion. Figure (e): polyanionic structure of $\text{Eu}_3\text{Sn}_2\text{P}_4$
 6 with polyhedral built from Sn and P atom.

7



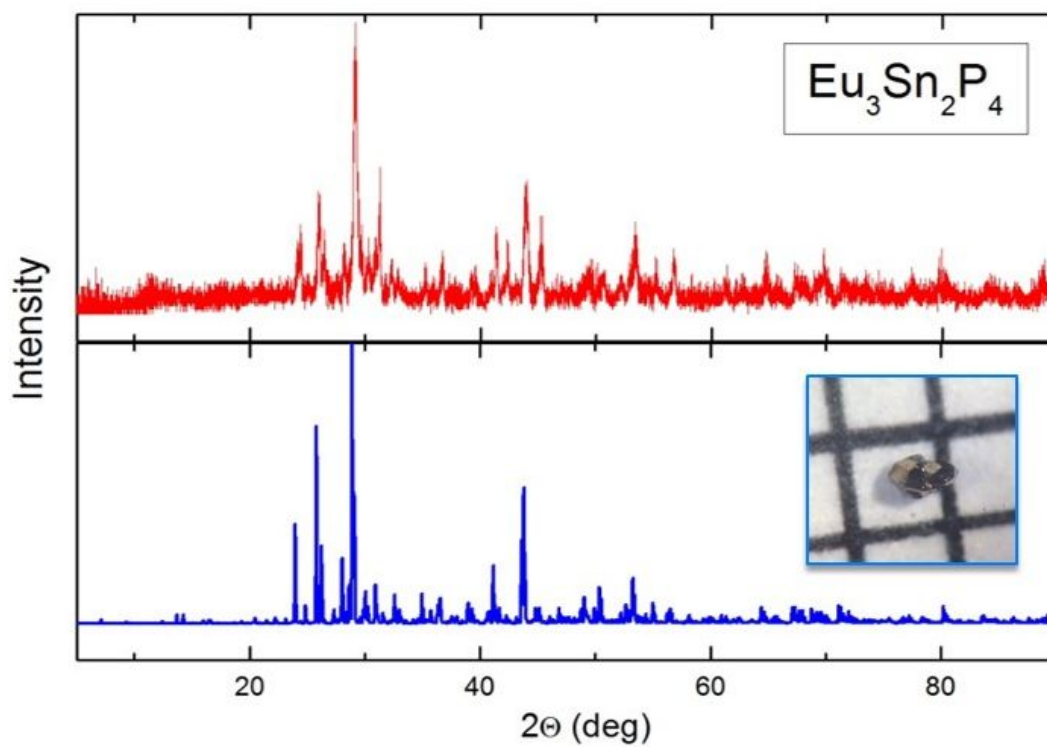
8

9

10

11

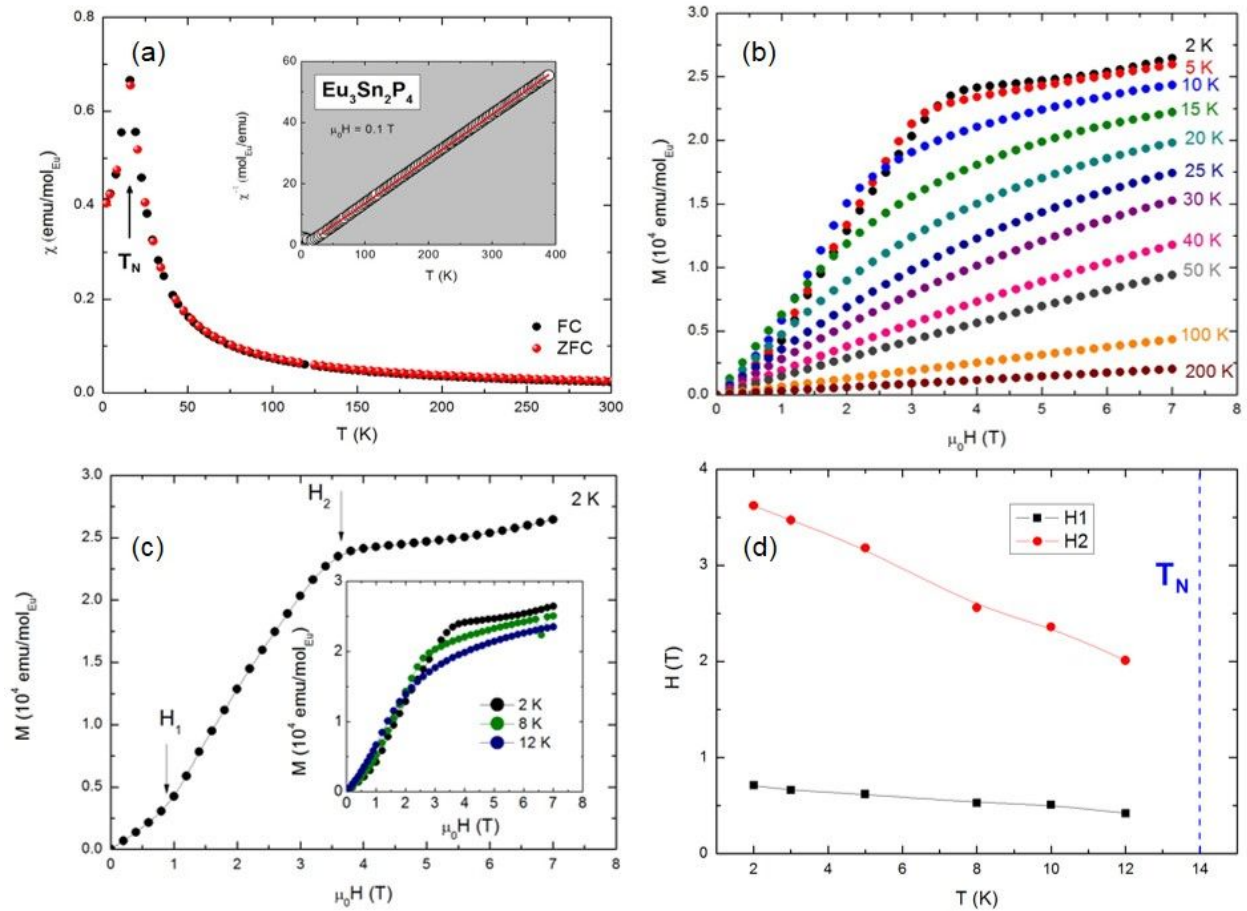
1 **Figure 2** The powder XRD pattern for $\text{Eu}_3\text{Sn}_2\text{P}_4$. The red and blue lines represent observed and
2 calculated intensities based on single crystal X-ray diffraction refinement, respectively. *Inset:* The
3 picture of $\text{Eu}_3\text{Sn}_2\text{P}_4$ single crystal.
4



5

1 **Figure 3.** (a) *Main panel:* magnetic susceptibility measured in ZFC (red circle) and FC (black
 2 circle) method. *Inset:* Temperature dependence of the magnetic susceptibility for $\text{Eu}_3\text{Sn}_2\text{P}_4$
 3 measured in a magnetic field of 0.1 T. The red line represents the Curie-Weiss fit, which is
 4 discussed in the text. (b) Magnetization versus applied magnetic field measured at several
 5 temperatures. (c) Field dependence of magnetization measured in the temperatures below T_N . The
 6 arrows emphasize metamagnetic-like transitions (d) The metamagnetic transition fields versus
 7 temperature.

8

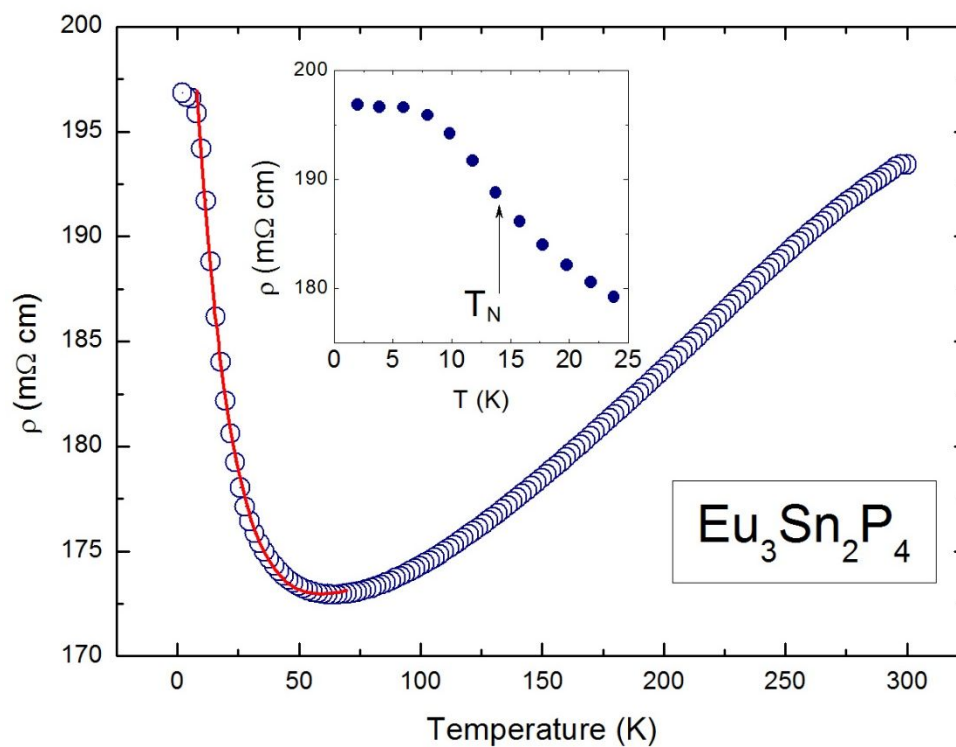


9

10

- 1 **Figure 4.** *Main panel:* The temperature dependence of resistivity for $\text{Eu}_3\text{Sn}_2\text{P}_4$ single crystal
2 measured without applied magnetic field. The red solid line represent the fit discussed in the text.
3 *Inset:* The low-temperature range of electrical resistivity.

4



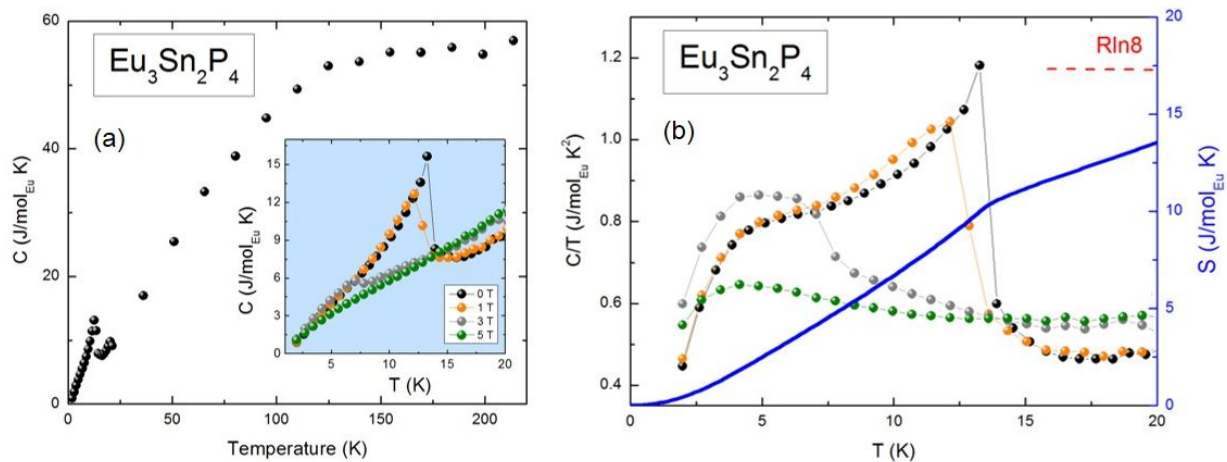
5

6

7

1 **Figure 5. (a) Main panel:** temperature dependence of specific heat measured without applied
2 magnetic field. *Inset:* low temperature range of specific heat versus temperature measured at 0, 1,
3 3 and 5 T. **(b)** low temperature specific heat over temperature (C/T) as a function of temperature
4 and calculated entropy.

5



6

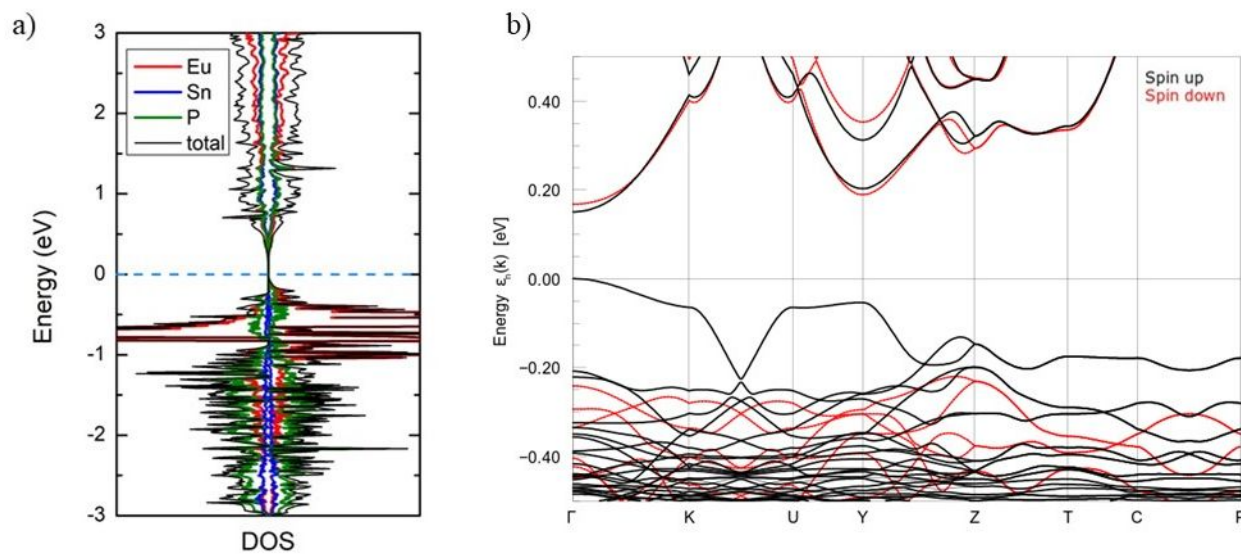
7

8

9

10

- 1 **Figure 6. (a)** Calculated total and partial DOS of $\text{Eu}_3\text{Sn}_2\text{P}_4$ with spin polarization. The energy
2 Fermi level is presented as a dashed blue line. **(b)** Band structure of $\text{Eu}_3\text{Sn}_2\text{P}_4$ calculated with
3 LSDA+ U near the Fermi level.



1 **Table 1.** Single crystal crystallographic data and structure refinement for $\text{Eu}_3\text{Sn}_2\text{P}_4$

Formula	$\text{Eu}_3\text{Sn}_2\text{P}_4$
F. W. (g/mol)	817.14
Space group, Z	$Cmca$ (#64), 24
a (Å)	24.882(3)
b (Å)	12.453(2)
c (Å)	18.493(2)
V (Å ³)	5730(1)
Absorption correction	Numerical
Extinction coefficient	0.0000157(9)
Θ range (°)	1.637 - 35.128
hkl ranges	$-40 \leq h \leq 40$ $-19 \leq k \leq 20$ $-29 \leq l \leq 29$
No. reflections, R_{int}	6427, 0.0725
No. independent reflections	242
No. parameters	132
R_1 , wR_2 (all I)	0.0354, 0.0494
Goodness of fit	1.029
Largest diff. peak and hole ($e^-/\text{Å}^3$)	-2.631, 2.081

2

1 **Table 2.** Atomic coordinates and isotropic displacement parameters of $\text{Eu}_3\text{Sn}_2\text{P}_4$. U_{eq} is defined as
 2 one-third of the trace of the orthogonalized U_{ij} tensor (\AA^2)

3

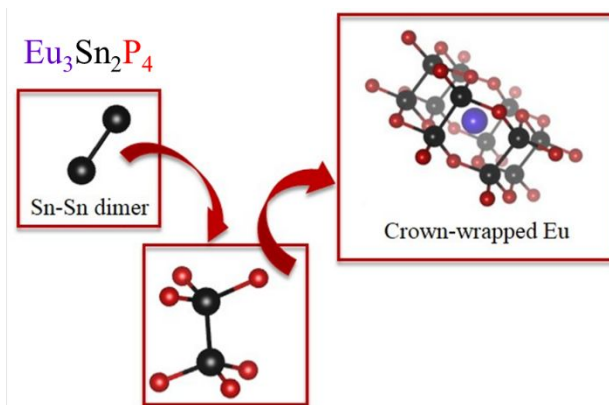
Atom	Wyckoff	Occupancy	x	y	z	U_{eq}
Eu1	4a	1	1/2	0	1/2	0.0092(1)
Eu2	16g	1	0.4166(2)	0.2117(3)	0.3685(2)	0.0099(6)
Eu3	8d	1	0.3247(2)	0	1/2	0.0106(8)
Eu4	8f	1	1/2	0.0619(4)	0.7291(2)	0.0112(9)
Eu5	16g	1	0.3314(2)	0.4521(3)	0.2411(2)	0.0102(6)
Eu6	4b	1	1/2	1/2	1/2	0.0155(1)
Eu7	16g	1	0.2445 (2)	0.2114(3)	0.3725(2)	0.0121(6)
Sn1	16g	1	0.4177(2)	0.2085(3)	0.5648(2)	0.0087(8)
Sn2	16g	1	0.3376(2)	0.4343(3)	0.4391(2)	0.0087(8)
Sn3	16g	1	0.4146(2)	0.1506(3)	0.1790(2)	0.0088(8)
P1	8f	1	1/2	0.2497 (2)	0.4863(1)	0.0096(4)
P2	16g	1	0.3346(6)	0.2013(1)	0.2526(9)	0.0100(3)
P3	16g	1	0.4131(7)	0.0254(1)	0.6160(8)	0.0099(3)
P4	8f	1	1/2	0.1869(2)	0.2521(1)	0.0100(4)
P5	16g	1	0.4232(6)	0.4574(1)	0.3639(9)	0.0107(3)
P6	16g	1	0.2466(6)	0.0389(1)	0.6276(9)	0.0104(3)
P7	16g	1	0.3335(6)	0.2442(1)	0.4899(9)	0.0099(3)

4

5

6

7

For Table of Contents Only

A novel antiferromagnetic semiconductor, $\text{Eu}_3\text{Sn}_2\text{P}_4$, has been discovered and prepared using the Sn self-flux method. The crystal structure shows that the six Sn-Sn dimers connected by P atoms form $\text{Sn}_{12}\text{P}_{24}$ crown-shape cluster with Eu atoms located in the center. Magnetization measurements indicate the antiferromagnetic ordering with an effective magnetic moment $\sim 7.41(3)\mu_{\text{B}}/\text{Eu}$, corresponding to Eu^{2+} . The electric resistivity reveals the energy gap ~ 0.14 eV.